2019

Charge Storage in WO^3 Polymorphs and Their Application as Supercapacitor Electrode Material

Vaibhav Lokhande

Abhishek Lokhande

Gon Namkoong
Old Dominion University, gnamkoon@odu.edu

Jin Hyeok Kim

Taeksoo Ji

Original Publication Citation

Lokhande, V., Lokhande, A., Namkoong, G., Kim, J. H., & Ji, T. (2019). Charge storage in WO_3 polymorphs and their application as supercapacitor electrode material. *Results in Physics, 12*, 2012-2020. doi:10.1016/j.rinp.2019.02.012

Results in Physics 12 (2019) 2012–2020

Contents lists available at ScienceDirect

Results in Physics

journal homepage: www.elsevier.com/locate/rinp

Charge storage in WO_3 polymorphs and their application as supercapacitor electrode material

Vaibhav Lokhande[a], Abhishek Lokhande[b], Gon Namkoong[c], Jin Hyeok Kim[b,*], Taeksoo Ji[a,*]

[a] Laboratory of Semiconductor Device Research, Department of Electronics and Computer Engineering, Chonnam National University, Gwangju 61186, South Korea
[b] Department of Materials Science and Engineering and Optoelectronics Convergence Research Center, Chonnam National University, Gwangju 61186, South Korea
[c] Department of Electrical and Computer Engineering, Old Dominion University, Applied Research Center, Newport News, VA 23606, USA

ARTICLE INFO

Keywords:
Supercapacitor
Tungsten oxide
Crystal phases
Surface controlled capacitance
Charge storage
Pseudocapacitive

ABSTRACT

Tungsten oxide is a versatile material with different applications. It has many polymorphs with varying performance in energy storage application. We report simple and facile way to synthesize four phases of tungsten oxide from same precursor materials only by changing the pH and temperature values. Monoclinic, hexagonal, orthorhombic and tetragonal phase obtained, were analyzed and tested for supercapacitor application. The electrochemical analysis of four phases indicates that the hexagonal phase is best-suited electrode material for supercapacitor. The hexagonal phase exhibits higher specific capacitance (377.5 Fg^{-1} at 2 $mV s^{-1}$), higher surface capacitive contribution (75%), better stability and rate capability of all four phases.

Introduction

Recently, owing to factors such as greenhouse gas emissions, pollution and the resulting global warming and climate change, cleaner forms of energy sources are being sought to mitigate the damage done to environment. This creates the necessity to develop new and better energy storages. Battery and fuel cell technologies are being investigated to make them a viable option. However, both technologies have their disadvantages and are not commercially viable to be used as large scale energy storage systems. The drawbacks are lower number of charge-discharge cycles, lower power density, lower rate capability and high cost. As the Ragone plot shows, both battery and fuel cells are high energy - low power devices whereas the demand for higher power density devices is increasing. Considering the recent market trends, there is a need of such a device which will bridge this gap. The consumer electronics, wearable technologies, portable electronics, electric vehicles etc. need higher power devices which will help them unleash their true potential. Supercapacitors (SC) or Ultracapacitors are such device which can fill in the void [1,2]. SC can handle the high power requirement better than battery without sustaining damage to itself. The pressure of high power can cause serious problems in batteries and thereby further reducing their life. As on the Ragone plot, SC have lower energy density but higher power density. Using SCs in tandem with battery they can ease of pressure on battery by providing peak power or with discovery of new electrode materials, SC can solely power the applications. The electrode materials used currently limit the capacity of the SC to 5–40 Wh Kg^{-1} and thus the application of SCs is more feasible in low energy consumption devices or using them in tandem with the battery.

SCs are classified into two types, electrochemical double layer capacitors (EDLC) and Pseudocapacitors. EDLC are mostly Carbon based devices. The electrode material used in the device is generally carbon or carbon derived material. Activated Carbon, Carbon Nano tubes, Graphene, Reduced Graphene oxide, etc. are most prominently used because of their large surface area [34,35]. The charge is stored by means of reversible ion adsorption on the surface of the electrode. Thus, these devices inherently have faster and higher charge-discharge cycles and higher power density. Since the ions are only adsorbed on the surface, the structural integrity of the electrode is maintained for longer period thereby providing longer life to the device. Surface adsorption also means the charge stored is easily and readily available which translates to higher power density however this also means lower energy density. Pseudocapacitors are devices which store charge faradaically by the fast reversible redox reactions at or near the surface of the electrodes. Transition metal oxides and conduction polymers exhibit this kind of charge storage behavior. Since the redox reactions occur at or near the surface, the pseudocapacitors are limited in their power density (still higher than battery) but they have higher energy density than the EDLC type. RuO_2, MnO_2, V_2O_5, IrO_2, Co O_4, Fe_2O_3) and hydroxides ($Ni(OH)_2$, $Co(OH)_2$, $Cu(OH)_2$ etc. and conducting polymers

* Corresponding authors.
E-mail addresses: jinhyeok@chonnam.ac.kr (J.H. Kim), tji@chonnam.ac.kr (T. Ji).

https://doi.org/10.1016/j.rinp.2019.02.012
Received 23 December 2018; Received in revised form 27 January 2019; Accepted 4 February 2019
Available online 08 February 2019

such as Polypyrrole, Polyaniline, Polythiophene etc. are used as electrode material for pseudocapacitors [3]. Tungsten oxide (WO_3) has also been used as pseudocapacitive electrode material. Tungsten oxide is an electrochemically stable n type semiconductor metal oxide with applications in various fields. After Deb's discovery of electrochromism in tungsten oxide, it gained huge attention from the scientific community and was extensively researched for its different properties. Tungsten oxide became a suitable candidate for electrochromic devices, gas sensing, photo catalysis etc. [4–7]. In recent years, many reports published confirm the feasibility of WO_3 as energy storage material [8,9,20–24,29–31]. High conductivity, desirable crystal structure and small radius have contributed to its electrochemical performance [10].

Tungsten oxide has at least five polymorphs and their respective crystal structure has notable influence on its electrochemical performance. Many reports on synthesis and characterization of WO_3 polymorphs have been published [11–20]. Various methods have been employed to synthesize WO_3, which include Chemical Vapor Deposition, Electrochemical deposition, Sol-Gel processing, Magnetron Sputtering, Chemical Precipitation method, Hydrothermal methods etc. [11–15]. Chacon et al. have reported synthesis and characterization of WO_3 polymorphs using solvo-thermal technique. They synthesized and characterized monoclinic, hexagonal and orthorhombic WO_3 by controlling the water content in the solvo-thermal method [16]. Kalhori et al. synthesized flower like WO_3 particles using hydrothermal method. By adding varying quantities of ammonium oxalate to precursor solution, they were able to synthesize orthorhombic and monoclinic WO_3 at different hydrothermal temperature and test the gas chromic response of WO_3 [17]. Huang et al. observed the effect of hydrothermal temperature on structure, morphology and phases of WO_3. They tested the as prepared samples for their photochromic properties [18]. Similarly, Nagy et al. have reported the effect of morphology and phases of WO_3 on its photocatalytic efficiency. They varied the pH to obtain different morphologies and phases of WO_3 [19]. Many reports on application of WO_3 as electrode material for supercapacitor are available [20–24,29–31]. However, the authors have only reported the performance of single phase of WO_3. Most commonly reported are monoclinic and hexagonal WO_3 [20–24]. According to the literature survey it is inferred that the hexagonal phase is most preferred phase due to its superior performance. Other phases are suitable electrode materials but their performance doesn't quite match that of the metastable hexagonal phase. Not many reports have been published which correlate the phase structure to energy storage capability [8,20,26]. In this paper, we report synthesis of 4 phases of WO_3 namely monoclinic, tetragonal, hexagonal and orthorhombic by hydrothermal method and analyze their electrochemical charge storage performance. The WO_3 samples were synthesized by varying the hydrothermal temperature and pH of the precursor solution. The variation of experimental parameters yielded many samples. All the samples were analyzed using X-ray diffraction and only the phase pure samples were utilized for further characterization and electrochemical testing.

Experimental section

Materials

Sodium Tungstate (Na_2WO_4, Sigma Aldrich) was used as tungsten precursor. Hydrochloric acid (HCl) was used to adjust the pH. Deionized water (DI) was used to dissolve the precursor, dilute the acid to desired molarity and for washing the final product. Ethanol was also used to wash and clean the final product of any impurities. Carbon cloth (CC) was used as substrate to slurry cast the as prepared powder. PVDF, Nafion and carbon black were used in slurry casting the samples onto the substrate.

Table 1
Sample synthesis parameters with resulting phase and particle shape.

Sample	pH	Hydrothermal Temperature	Phase	Shape
W1	0.5 & 1	180	Monoclinic	Cube
W2	3	160	Hexagonal	Cube
W3	2	180	Orthorhombic	Nano rods
W4	1	200	Tetragonal	Cubic Plate

Synthesis of WO_3 powder and electrode preparation

In a typical synthesis, 0.6 g of Na_2WO_4 was dissolved in 10 ml DI by magnetically stirring for 10 min at room temperature. 3 M HCl was added drop by drop to the Na_2WO_4 solution while stirring it until the desired pH value was reached. Once the pH value was achieved the complete mixture was kept under stirring until it turned milky or yellowish depending on the pH value. This final solution was transferred into a Teflon liner (100 ml) and then sealed in an autoclave. The hydrothermal temperature was set and autoclave was heated in the oven for 12 h. In these experiments, time was kept constant. At each pH values 0.5, 1, 2 and 3, experiments were conducted at 160, 180 and 200 °C yielding 12 samples. The phase pure samples were selected for further analysis. The autoclave was allowed to cool down naturally in the oven. The precipitate collected was washed alternatingly with DI and ethanol for three times. The samples (powder) were centrifuged and dried at 80 °C in an oven for 6 h. The synthesis parameters of the phase pure samples are listed in the Table 1 below.

The samples were ground in mortar and pestle and mixed with PVDF and Carbon black in 85:15:5% w/w (Sample: PVDF: Carbon black). 3 ml of Nafion was added to the mixture to form a slightly viscous paste. Carbon cloth (2 × 2 cm) was dipped and ultra-sonicated in the viscous paste for 30 min. The substrate was removed and placed on the table. The viscous paste was casted onto the substrate using 5 ml dropper. Carbon cloth was left for drying in a vacuum oven at 60 °C for 18 h. The as prepared samples used for electrochemical testing. The weight of Carbon cloth was recorded before and after slurry casting. The mass loading of the active material was calculated to 1.5 mg cm^{-2}, 0.8 mg cm^{-2}, 1.5 mg cm^{-2}, 1 mg cm^{-2} for samples W1, W2, W3 & W4 respectively.

Characterization of materials

The X-ray diffraction analysis (XRD) was done using Bruker AXS D8 Advance Model with copper radiation (Kα with λ = 1.54 Å). XRD spectra were recorded for 2θ values ranging from 10° to 90° at a scanning rate of 4°/s. The surface morphology was characterized using field emission scanning electron microscopy (FE-SEM, Model: JSM-6700F, Japan). X-ray photoelectron Spectroscopy was performed by VG Multilab 2000 to obtain information regarding the oxidation state of the elements. XPS is fitted by Gaussian distribution method. The high-resolution transmission electron microscopy image (HR-TEM) was obtained using a high resolution JEOL-3010 microscope. The samples were prepared by dispersing the powder in ethanol and putting a drop of suspension onto a carbon-coated copper grid. Raman Spectroscopy was performed using JASCO NRS-5100 with 532.13 nm Laser wavelength. OHAUS Explorer EX125 (0.01 mg) analytical balance was used to precisely measure the weight of substrate before and after hydrothermal deposition.

Electrochemical measurements

The electrochemical characterization was done using Wonatech WBCS3000S. In order to decide the best performance for supercapacitor application, all the electrochemical measurements were carried out in three electrode system, which contain the as prepared electrodes as

working electrodes, saturated calomel electrode (SCE) as reference electrode and Pt as counter electrode in 1 M H_2SO_4 electrolyte.

Result and discussion

The formation of WO_3 can be explained through the equations [19].

$$Na_2WO_4 \rightarrow 2Na^+ + WO_4^{2-} \quad (1)$$

$$WO_4^{2-} + 2H^+ \rightarrow H_2WO_4 \quad (2)$$

$$H_2WO_4 \rightarrow WO_3 + H_2O \quad (3)$$

The first step is protonation of tungstate ions upon acidification to form milky white or yellowish tungstic particles. The tetrahedral H_2WO_4 further undergoes hydration to form octahedral crystalline complex with water molecule held by weak intermolecular forces. This step is important because during this step, the morphology and size could be controlled by means of additives but in absence of such agents, influence of pH and temperature is more dominant. The last step is the condensation or removal of water from the tungstic particles. As the water is removed from the structure, the W—O bonds reform and enable O atoms to interconnect and stack together leading to phase transition. More compact, low energy and stable phase is preferred. The hydrothermal conditions and the degree of dehydration results in different polymorphs of WO_3.

Control of particle size by pH variation

As evident from the equation H^+ play important role in formation of WO_3. This points to the fact that pH is a crucial factor in crystal nuclei formation. The degree of supersaturation determines the rate of formation of crystal nuclei and crystal growth. Highly acidic system has higher concentration of H^+ ions and thus the rate of crystal nuclei formation is also high. Large number of crystal nuclei are formed which subsequently determine the size of the particle. Smaller sized particles are formed in this situation. On the contrary, low level of supersaturation i.e. less acidic system the particle size is larger. The monoclinic and orthorhombic phases are formed at 180 °C hydrothermal temperature and pH value 0.5 and 1, 2 respectively. The hexagonal phase was formed at 160 °C temperature and at pH 3. The particle size of the samples, as seen from the SEM images and HRTEM Fig. S9, shows increasing trend as we transition from monoclinic to orthorhombic and to hexagonal phase. Tetragonal phase was synthesized at 200 °C for pH value 1. With the supply of more energy to reaction system, the W-O bonds reform themselves to realign in crystal system with lower energy level and become more stable.

The structural and phase analysis of W1, W2, W3 and W4 samples synthesized with different pH and temperature values are performed by recording the X-ray diffraction pattern as shown in Fig. 1 followed by the Rietveld refinement method in the structural fitting mode. According to the JCPDS cards 00-005-0363, 00-0033-1387, 00-020-1324 and 00-005-0388 the W1, W2, W3 and W4 sample exhibits the monoclinic, hexagonal, orthorhombic and tetragonal crystal structure, respectively. The detailed structural evaluation of these sample are investigated by means of the Rietveld refinement in FullProf suit with structural fitting profile matching mode in corresponding space symmetry (SI Fig. S7 and 8). The refinement parameters of all sample shows that all sample exhibit single phase WO_3. Table 2 shows that the W1 sample exhibit very stable phase in monoclinic structure having *P21/a* space symmetry. The large distortion is observed on WO_6 octahedron of W3 sample which exhibit the orthorhombic crystal structure. Table 3 shows that the W3 sample exhibit the maximum value of the W—O bond length which promotes the electron hopping mechanism via oxygen vacancies. Hence, the probability to enhance the electrochemical property of WO_3 sample maximizes.

The scanning electron microscopy (SEM) is used to probe the surface morphology of the all WO_3 samples. Fig. 2 shows the SEM images of the all WO_3 sample at 50kX and 150kX resolution. In general all the samples exhibit well porous surface morphology. For the W1 (Fig. 2a, b) and W3 (Fig. 2e, f) sample, the nanocubes of different sizes are observed. The size of the nanocube of sample W1 is comparatively smaller than the sample W3. This may be due to preferred structural elongation of the lattice along one direction in orthorhombic structure. W2 (Fig. 2c, d) and W4 (Fig. 2g, h) samples show formation of plates like morphology with spherical shaped particles sprinkled all over the surface. W2 sample has formation of hexagonal plates while W4 shows formation of cubic plates.

In order to corroborate the structural analysis of XRD and morphological evolution by SEM, the transmission electron microscopic measurement of these samples are performed along with the complementary study of the selective area electron diffraction (SAED) study, inset pictures in Fig. 3. In addition, the effect of the variation of pH is clearly seen in the TEM images of the samples in Fig. 3. The grains were textured into the respective morphology of the W1, W2, W3 and W4 samples. The cube shaped grains are observed for W1 (Fig. 3a) and W3 (Fig. 3c) samples while hexagonal like grains are observed in W2 (Fig. 3b) sample. Partially distorted surface morphology is observed for the W3 and W4 (Fig. 3d) samples due to the incomplete orientation of the lattice.

Raman spectroscopy was performed to identify distinguishable peak pattern for the four phases of tungsten oxide. As shown in the Fig. 4, the peaks between 200 and 400 cm^{-1} correspond to bending of O—W—O bonds while the peaks between 700 and 900 cm^{-1} correspond to the stretching of the O—W—O bonds. The peak in the region 950–980 cm^{-1} is attributed to the terminal bond stretching (W═O) [10].

The monoclinic structure is distorted ReO_3 type structure and consists network of WO_6 octahedra. Two maxima are observed in the stretching regions. The two peaks are centered at 715 and 809 cm^{-1}. No peak is observed in the 950–980 cm^{-1} region suggesting the anhydrous nature of the sample [25]. The peak at 331 cm^{-1} which is observed in the bending region corresponds to the bending of O—W—O bonds. The second sample, W2, has hexagonal structure which is formed by corner sharing of WO_6 octahedra forming a six member hexagonal ring. The stacking of these ring in 001 direction leads to the formation of hexagonal tunnels. A peak at 340 cm^{-1} is attributed to the O—W—O bond bending. Further, the Raman spectra shows two maxima, one at 684 cm^{-1}, a big shift from the monoclinic phase, due to the open structure arrangement of the crystals and second maximum centered at 810 cm^{-1} [26]. The peak at 948 cm^{-1} is attributed to terminal W═O bond stretching. W3 sample has bending peak at 331 cm^{-1} and stretching peaks at 712 and 810 cm^{-1} [26]. The tetragonal phase has a peak at 330 cm^{-1} (O—W—O bending) and two peaks at 713 and 809 cm^{-1} (O—W—O stretching) [27]. The bending peaks do not show much variation except in case hexagonal phase. In the stretching region, the 800 band is less indicative of phase transition than the 700 band. The variation in the 700 band is more prominent and sensitive to phase transition.

The surface chemistry and the oxidation state of tungsten was determined using XPS analysis. In the survey scan of four samples as observed in Fig. 5a, only W, O, and C were present suggesting the samples contained no impurities. All four samples show well defined peaks and confirm the formation of tungsten oxide (WO_3). Fig. 5b shows W 4f core scans. The positions of W 4f5/2 and W 4f7/2 peaks confirm the +6 oxidation state of Tungsten (W). The O 1s scan depicted in Fig. 5c shows peaks with similar binding energies to that of O—W bond [19]. A shoulder peak at around 533 eV is observed in samples 2, 3 and 4 suggesting presence of O—H bond.

Electrochemical characterization

The charge storage behavior and mechanism in the four phases of tungsten oxide was studied using cyclic voltammetry. The potential

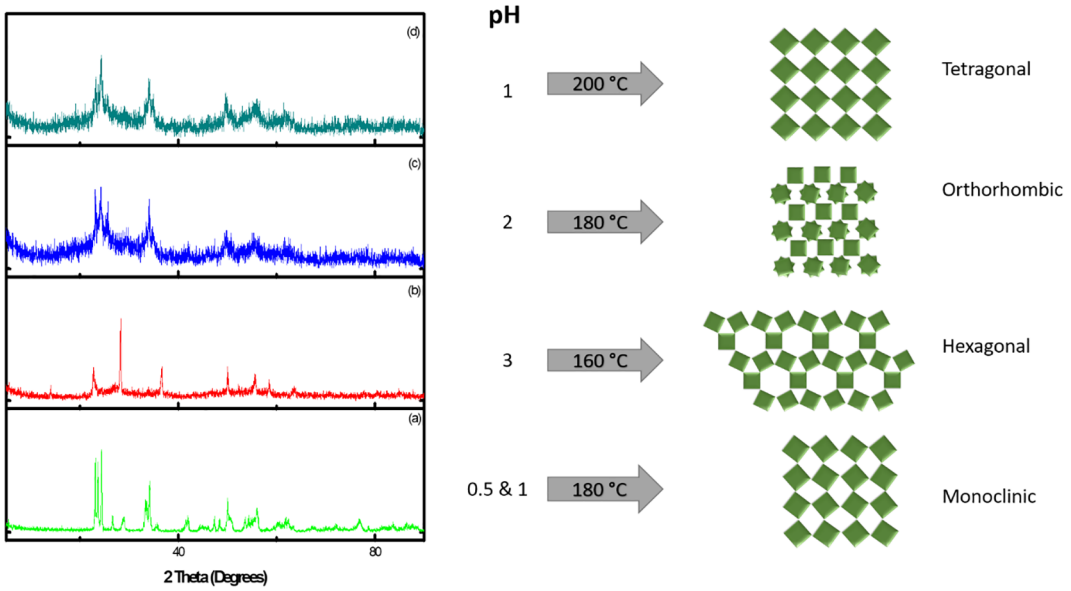

Fig. 1. XRD pattern of W1, W2, W3 and W4 samples with their corresponding crystal structure.

Table 2
Rietveld refinement parameters of WO_3 samples.

Sr. No.	Sample ID	Crystal Structure	Space Group	R_p	R_{wp}	χ^2
1	W1	Monoclinic	P21/a	9.21	15.4	3.2
2	W2	Hexagonal	P6/m m m	10.17	15.69	3.6
3	W3	Orthorhombic	P c n b	10.58	19.1	4.3
4	W4	Tetragonal	P4/n m m	9.88	17.5	3.9

window for the active material was determined to be from −0.6 to 0.2 V vs S.C.E by scanning the electrodes in three electrode setup at $2\,mV\,s^{-1}$ scan rate. Shape of the curve, hydrogen evolution and complete pair of redox peaks were used to restrict the potential window. There is considerable difference in the shape of CV curves of the WO_3 phases as observed in Fig. 6. During the cathodic cycle, one can observe the onset of hydrogen evolution near −0.6 V. The current switching between (cathodic to anodic) is faster in samples W2 and W3. W4 shows a little delay while sample W1 has a considerable delay. Considering the shape and the current switching, the hexagonal (W2) and orthorhombic (W3) WO_3 show behavior similar to that of an ideal supercapacitor. The specific capacitance of the four samples at different scan rate are listed in the Table 4. The following formula was used to calculate the specific capacitance from the CV curves.

$$C = \frac{\int I(v)dv}{mv\Delta V} \tag{4}$$

where ∫ I (v) dv is the area under the CV curve, m is the mass of active material in grams, v is the scan rate in millivolts per second and ΔV is the potential window in volts. The hexagonal phase W2 ($377.5\ Fg^{-1}$) sample shows the highest capacitance at $2\,mV\,s^{-1}$ scan rate followed by W4 ($368.75\ Fg^{-1}$), W3 ($331\ Fg^{-1}$) and W1 ($325\ Fg^{-1}$).

As the scan rate increases, the specific capacitance of all samples decreases at different rate. The W4 sample shows the highest drop in capacitance (83%) when the capacitance at lowest $2\,mV\,s^{-1}$ and highest scan rate $100\,mV\,s^{-1}$ are compared. While the W2 sample shows the least drop of 64%. The contribution in charge storage from carbon cloth substrate was found to be negligible. CV of bare carbon cloth (substrate) in 1 M H_2SO_4 electrolyte at $50\,mV\,s^{-1}$ scan rate, as depicted in SI Fig. S1, suggests insignificant contribution to total charge stored in the samples. To understand further the nature of charge storage mechanism the electrochemical kinetic analysis was performed. First, the charge storage mechanism of WO_3 is considered. The charge storage in WO_3 is due to the intercalation of protons and injection of electrons and transition of W^{6+} to W^{5+} and vice versa.

$$WO_3 + xH^+ + xe^- \leftrightarrow HWO_3 \tag{5}$$

Form the experimental data, the variation in the specific capacitance of the samples at different scan rates suggests that the total charge stored is contribution of two distinct charge storage methods namely, surface capacitive and diffusion limited. The current (i) at particular potential (V) follows power law relationship with the scan rate (v). The equation describes the power law relationship:

$$i(V) = av^b \tag{6}$$

where a, b are adjustable constants. The range of values which b can take are limited within 0.5 to 1. If the value of b is 0.5 then the current is controlled by semi-infinite linear diffusion of ions (like in battery) and if the value is 1 then the current is surface controlled (EDLC and Pseudocapacitive). Thus, closer the value of b to 1, more ideal supercapacitive behavior of the material. The current values at the reduction peak potentials present in the CV curves are considered. The peak positions are not exactly same for all the samples. Samples W1 and W4

Table 3
Crystal structure, lattice parameters, Bond length and unit cell volume of WO3 samples.

Sr. No.	Sample ID	Crystal Structure	Lattice parameters						W - O (Å)	Unit cell Volume (V) (Å^3)
			a (Å)	b (Å)	c (Å)	α (deg.)	β (deg.)	γ (deg.)		
1	W1	Monoclinic	7.30	7.52	3.84	90	90.76	90	2.51	211.20
2	W2	Hexagonal	7.29	7.29	3.89	90	90	120	4.23	179.03
3	W3	Orthorhombic	7.33	7.57	7.74	90	90	90	1.84	429.85
4	W4	Tetragonal	5.24	5.24	3.93	90	90	90	1.01	107.81

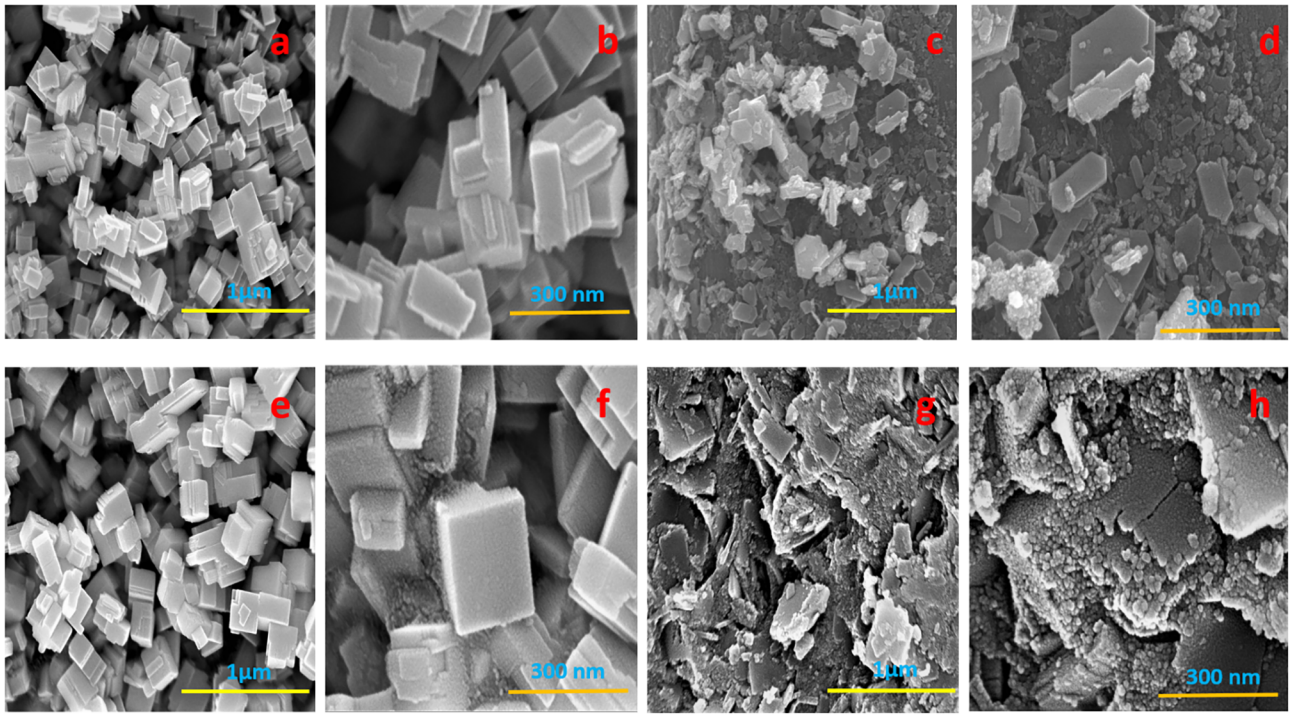

Fig. 2. SEM images at 50kX and 150kX magnifications of W1 (a, b), W2 (c, d), W3 (e, f) and W4 (g, h) samples, respectively.

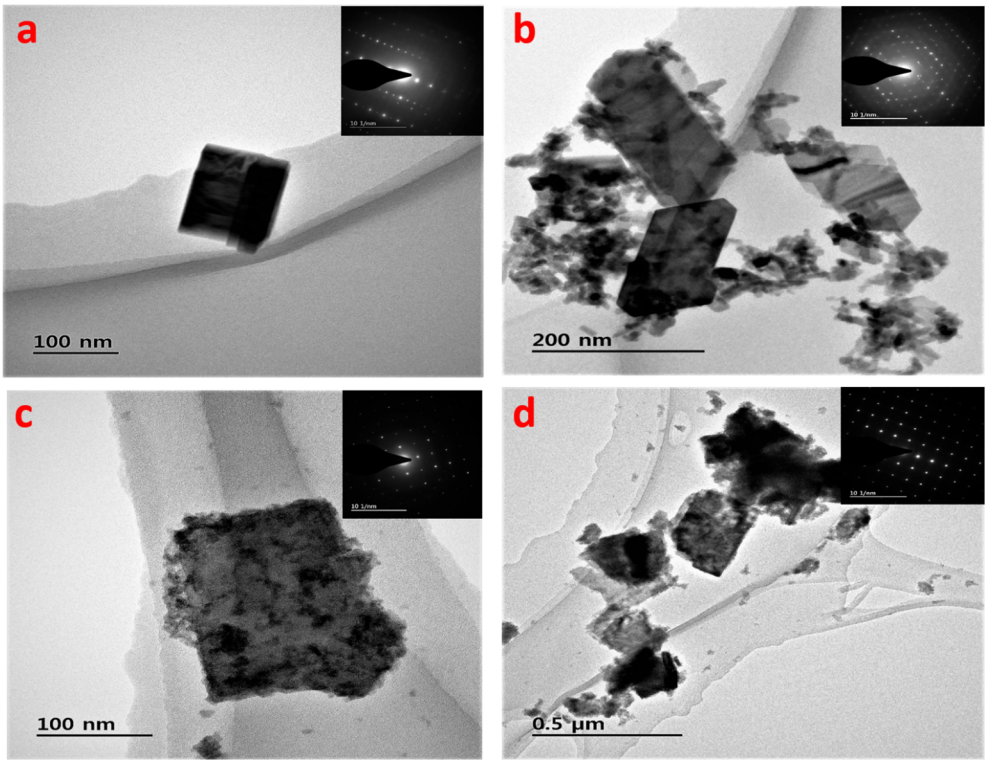

Fig. 3. TEM images of W1 (a), W2 (b), W3 (c) and W4 (d) with inset images of SAED pattern.

show cathodic peaks at fairly the same potentials at −0.1 and −0.35 V. In sample W3, only one peak at −0.5 V is distinguishable. Similar peak is observed in sample W2 in addition to peak at −0.1 V. The plot of the log (*v*) to log (*i*) gives the value of *b*. The plot is shown in SI Fig. S2. In case of W2 and W3 the values are very close to 1 hence suggesting the supercapacitive behavior. However, for W1 and W4 the values of *b* suggest battery type behavior. To analyze and categorize the charge storage contribution, the analytical model proposed by Dunn et al. was adopted [28]. The model can be summarized in the equation below.

$$i(v) = k_1 v + k_2 v^{1/2} \tag{7}$$

where k_1 and k_2 are the coefficients of the diffusion controlled and surface capacitive charge respectively. For the kinetic analysis only the CV curves at lower scan rates are considered (50 and 100 mV s^{-1} are

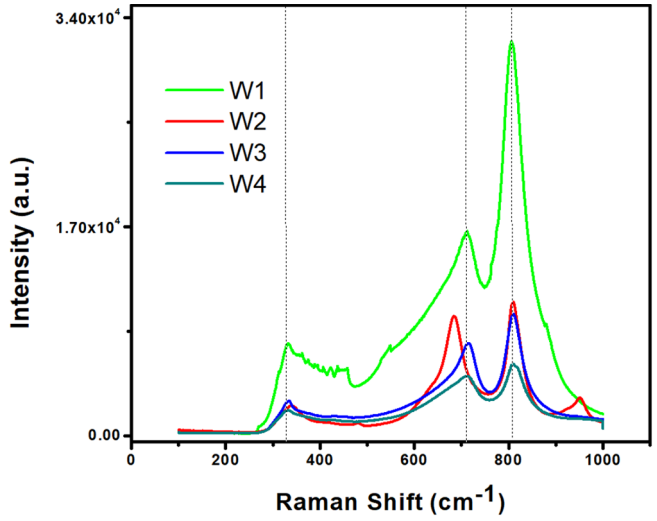

Fig. 4. RAMAN spectra of W1, W2, W3 and W4 samples.

excluded) because at higher scan rates the effect of factors such as ohmic losses, polarization and considerable shift in peak positions are not compensated for in the model. The total charged stored at different scan rates is calculated as explained in SI and plotted against inverse of the square root of scan rate. The plot was linearly fitted and extrapolated to find the contribution of surface capacitive charge (Q_s) as shown in SI Fig. S4. The remaining charge stored was concluded to be contributed from ion diffusion mechanism (Q_d) into the material. The CV curves plots for the samples W1, W2, W3 and W4 for 2–20 mVs^{-1} scan rate range are shown in SI Fig. S3. The value of surface capacitive contribution is assumed to be independent of scan rate (for lower scan rates) according to the model. As observed, the total charge stored decreases with increase in scan rate. This is because diffusion controlled charge contribution gets subdued with increase in scan rate. Ions diffusion into WO_3 lattice is time dependent and with increasing scan rate, lesser time is available. The contribution from the surface capacitive reactions increases with increase in scan rate and dominates the total contribution at higher scan rates. At 2 mVs^{-1}, the surface capacitive contribution was 34, 45, 43 and 21% for W1, W2, W3 and W4 samples, respectively. This contribution increased up to 64, 75, 70 and 63% for 20 mVs^{-1} scan rate. The charge contribution from the two separate processes is shown in Fig. 7. Crystal structure and morphology play a vital role in charge storage within the material. Sample W2, hexagonal phase has well defined hexagonal tunnels for easy ion intercalation. The elongation of the structure provides better-unobstructed pathways. Similarly, sample W3 has larger unit cell volume as calculated in Table 3. This helps in easy movements of ions within the crystal structure and contributes towards better electrochemical performance. Thus, by the virtue of their crystal structure and morphology, samples W2 and W3 are expected to perform better. Their physical characteristics are more conducive for fast surface reaction.

Stability is an important performance parameter for supercapacitor electrode material. A supercapacitor has to undergo many more charge-discharge cycles than a battery. In our studies we observed the stability of all the samples over 4000 cycles scanned at 20 $mV\,s^{-1}$ scan rate. Stability is greatly impacted by the morphology of the material. In our case though the morphology of all the samples is more or less similar. However, the stability of the samples vary greatly as shown in Fig. 8a. The capacitance retention for W2 and W3 samples is 90 and 94% respectively. Since the surface capacitance plays dominant role in the charge storage, the structure of the material is not greatly affected. Samples W1 and W4 show much higher loss in capacitance. The capacitance retention for the samples is 82 and 76% respectively. The diffusion of ions deeper into the material has profound effect on the structure of the material and thus its stability. Diffusion mechanism into the WO_3 lattice leads to structural degradation and consequently the cyclic capability of the sample suffers. EIS study was conducted to analyze the impedance of the samples. EIS was performed before the electrochemical analysis. The EIS was performed by measuring the impedance spectra in the frequency range of 100 KHz to 0.1 Hz at open circuit potential with ac perturbation of 10 mV. The Nyquist plot is shown in Fig. 8b.

At very high frequencies, the intercept on the x-axis i.e. on the Z real

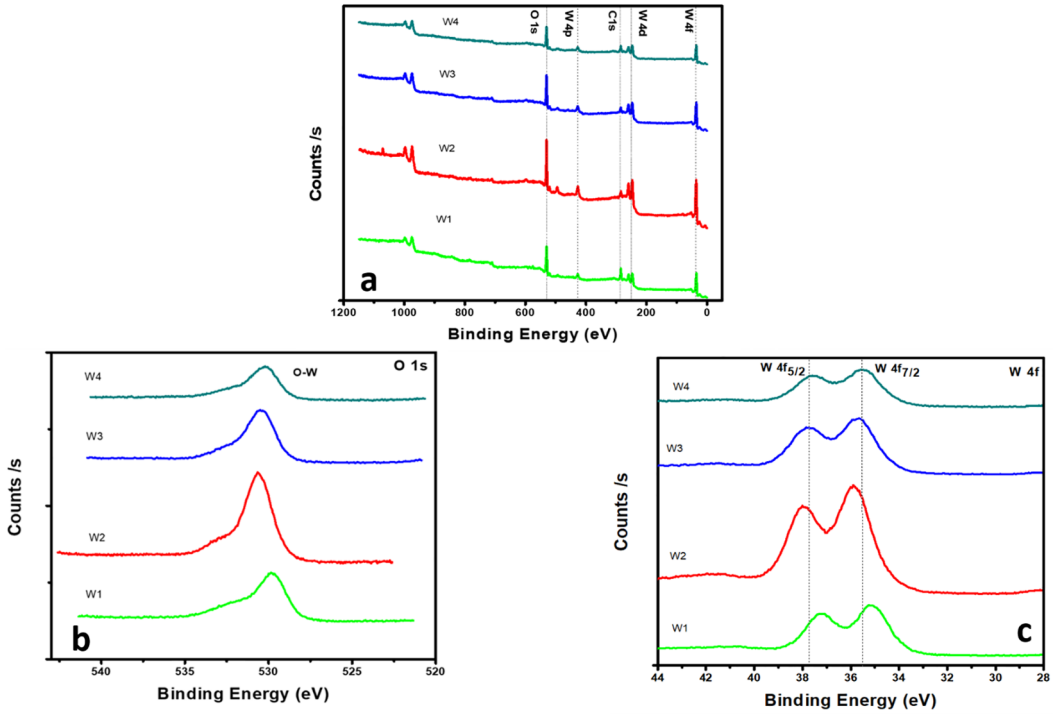

Fig. 5. (a) Survey spectrum (b) W 4f scans and (c) O 1s scans of samples W1, W2, W3 and W4 samples.

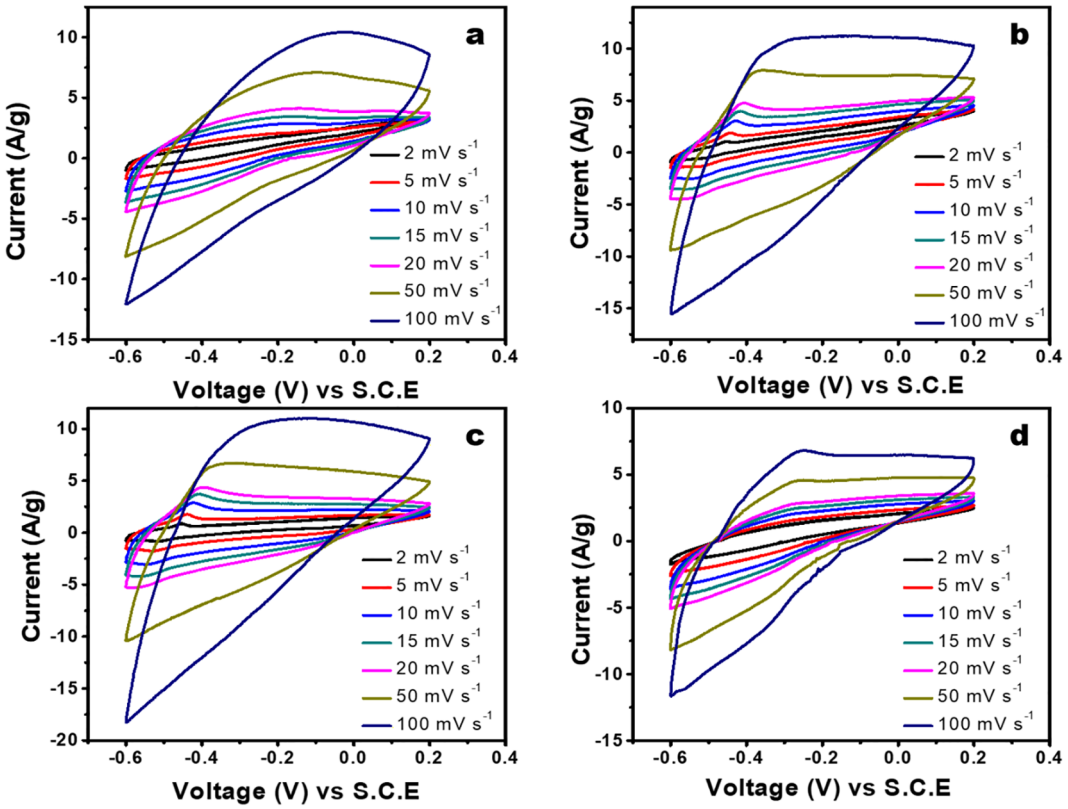

Fig. 6. CV curves of samples (a) W1, (b) W2, (c) W3 and (d) W4 at scan rate 2–100 mV s^{-1}.

Table 4
Capacitance of WO_3 samples at different scan rate.

Sample	Scan rate (mV s^{-1})							Capacitance Fg^{-1}
	2	5	10	15	20	50	100	
W1	325	240	220	190	175	125	90	
W2	377.5	316.667	275	250	229.166	166.66	133.33	
W3	331	250	227	212.12	204	135.41	104.166	
W4	368.75	232.5	168.7	140	123.75	82.5	61.25	

axis indicates R_s (Series resistance/intrinsic resistance). This is the cumulative resistance of intrinsic resistance of the substrate, ionic resistance of the electrolyte and the interfacial resistance at the substrate and active material interface. Small semicircle is observed in the high frequency region. This arises due to the faradaic charge transfer process and double layer capacitance and hence is called as R_{ct} (charge transfer resistance). The low frequency region has a sloped line referred as Warburg diffusion resistance W. Warburg diffusion indicates the frequency dependent ion diffusion in the electrolyte to electrode. The EIS data acquired was fitted using Zman Software. The data and equivalent circuit diagram is shown in SI Fig. S5 and S6. The sample W2 has the smallest Rs value 1.59 followed by W3, W1 and W4 respectively, indicating that there is better contact between active material and the substrate. Similarly, the Rct value for W2 is 1.59, which is the smallest of all samples indicating fast kinetics and easy transfer of charge [32,33]. The Z phase angle at lower frequencies, as shown in the bode plot SI Fig. S5, confirm that the sample W2 and W3 exhibit capacitive behavior. The sample W1 and W4 with Z phase angle closer to 45 suggest battery like behavior. All the parameters of the equivalent circuit for all the samples are given in SI Table S2. Thus, the EIS data analysis further strengthens our findings about the nature of charge storage in different phases of tungsten oxide.

Conclusion

We report synthesis of tungsten oxide polymorphs by simply varying the pH and hydrothermal temperature. Monoclinic, hexagonal, orthorhombic and tetragonal phases of tungsten oxide obtained by hydrothermal route are studied for the charge storage mechanism in each phase. The contribution from two different charge storage mechanism (i) surface capacitive (ii) diffusion limited were analyzed and quantified. Based on the electrochemical performance, hexagonal and orthorhombic phases are ideally suited for supercapacitor application. They exhibit pseudocapacitive behavior with better cyclic stability, rate capability and higher specific capacitance than the monoclinic and tetragonal phase. More open structures and wide tunnels enable fast, reversible intercalation of ions in hexagonal and orthorhombic phase. Monoclinic and tetragonal phase prominently exhibit diffusion type charge storage mechanism, suitable for battery application. Tungsten oxide can be used as energy storage material with hexagonal phase being most suitable as supercapacitor active electrode material.

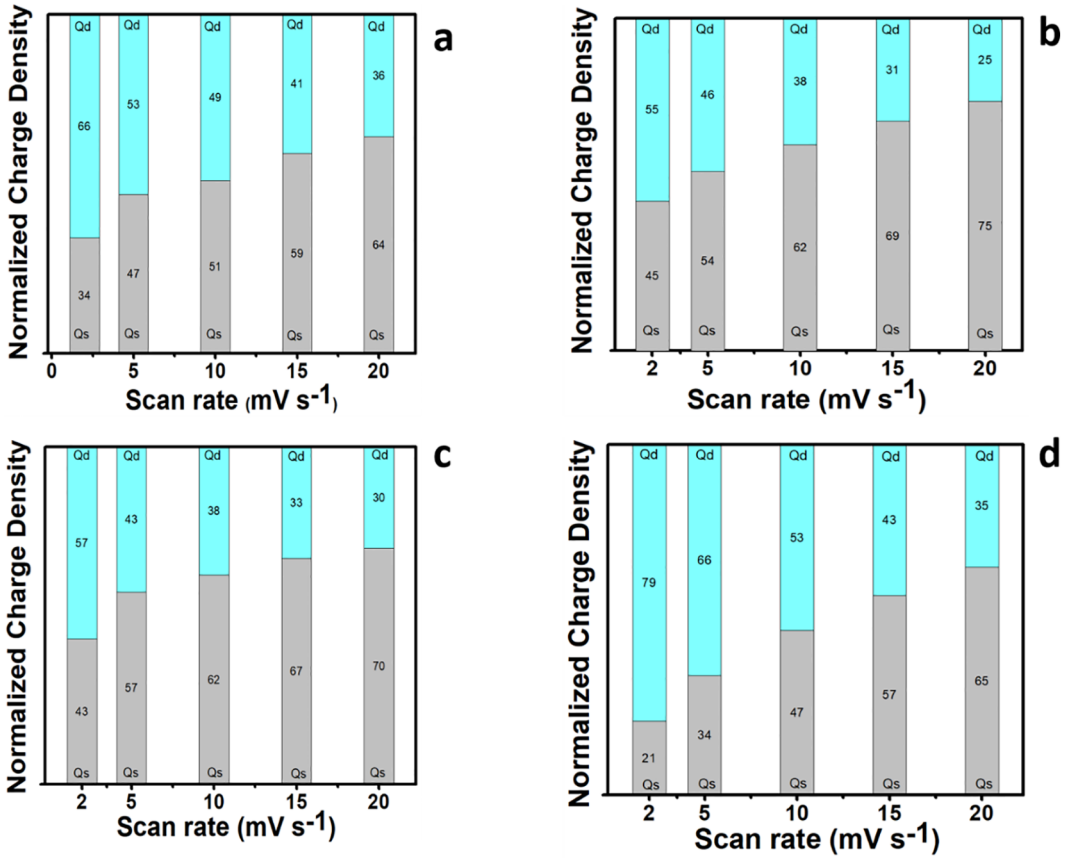

Fig. 7. Surface capacitive and diffusion limited contribution for (a) W1, (b) W2, (c) W3 and (d) W4.

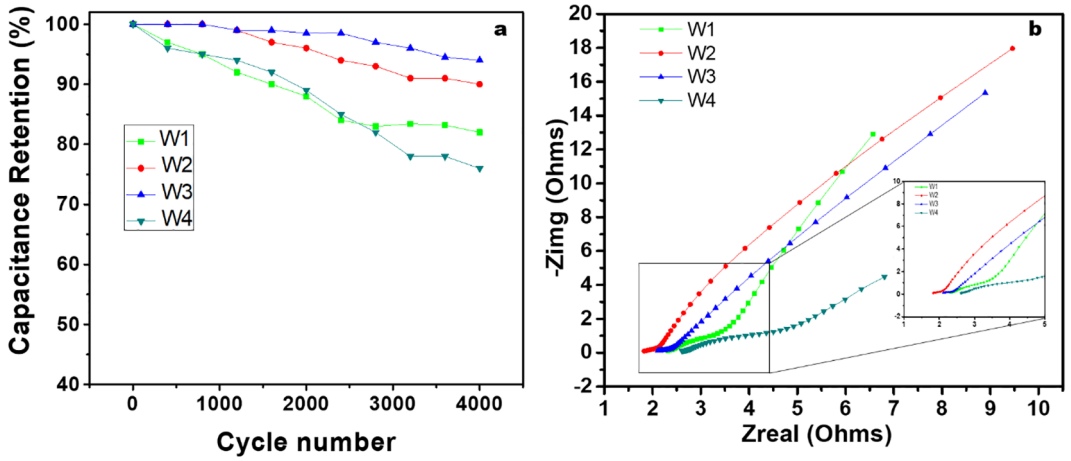

Fig. 8. (a) Cyclic stability study for 4000 cycles and (b) Nyquist plot of W1, W2, W3 and W4 samples (inset magnified image of selected area on graph).

Acknowledgement

This work was partially supported by the Basic Science Research Program through the National Research Foundation of Korea funded by the Ministry of Education (NO. 2018048610) and by the Human Resources Development Program (No. 20164030201310) of the Korea Institute of Energy Technology Evaluation and Planning (KETEP) Grant funded by the Korean Government Ministry of Trade, Industry and Energy.

Appendix A. Supplementary material

Supplementary data to this article can be found online at https://doi.org/10.1016/j.rinp.2019.02.012.

References

[1] Di Chen, Wang Qiufan, Wang Rongming, Shen Guozhen. Ternary oxide nanostructured materials for supercapacitors: a review. J Mater Chem A 2015;3:10158.
[2] Burke A. Ultracapacitors: why, how, and where is the technology. J Power Sources 2000;91:37.
[3] Lokhande VC, Lokhande AC, Lokhande CD, Kim JH, Ji TS. Supercapacitive composite metal oxide electrodes formed with carbon, metal oxides and conducting polymers. J Alloy Compd 2016;682:381–403.
[4] Sanrato C, Odziemkowski M, Ulmann M, Augustynski J. Crystallographically oriented mesoporous WO_3 films: synthesis, characterization, and applications. J Am Chem Soc 2001;123:10639–49.
[5] Baeck SH, Choi KS, Jaramillo TF, Stucky GD, McFarland EW. Enhancement of photocatalytic and electrochromic properties of electrochemically fabricated

mesoporous WO_3 thin films. Adv Mater 2003;15:1269.
[6] Srinivasan A, Miyauchi M. Chemically stable WO_3 based thin-film for visible-light induced oxidation and superhydrophilicity. J Phys Chem C 2012;116:15421–6.
[7] Mi Q, Zhanaidarova A, Brunschwig BS, Gray HB, Lewis NS. A quantitative assessment of the competition between water and anion oxidation at WO_3 photoanodes in acidic aqueous electrolytes. Energy Environ Sci 2012;5:5694.
[8] Yang P, Sun P, Du L, Liang Z, Xie W, Cai X, et al. Quantitative analysis of charge storage process of tungsten oxide that combines pseudocapacitive and electrochromic properties. J Phys Chem C 2015;119:16483.
[9] Conway BE. Electrochemical supercapacitors: scientific fundamentals and technological applications. New York: Kluwer Academ-ic/Plenum Publishers; 1999.
[10] Xu J, Ding T, Wang J, Zhang J, Wang S, Chen C, et al. Tungsten oxide nanofibers self-assembled mesoscopic microspheres as high performance electrodes for supercapacitor. Electrochim Acta 2015;174:728–34.
[11] Hutchins MG, Abu-Alkhair O, El-Nahass MM, Abd El-Hady K. Structural and optical characterisation of thermally evaporated tungsten trioxide (WO_3) thin films. Mater. Chem. Phys. 2006;98:401.
[12] Mahan AH, Parilla PA, Jones KM, Dillon AC. Hot-wire chemical vapor deposition of crystalline tungsten oxide nanoparticles at high density. Chem Phys Lett 2005;413:88–94.
[13] Deepa M, Srivastava AK, Sharma R, Govind SN, Shivaprasad SM. Microstructural and electrochromic properties of tungsten oxide thin films produced by surfactant mediated electrodeposition. Appl Surf Sci 2008;254:2342.
[14] Yoo SJ, Jung YH, Lim JW, Choi HG, Kim DK, Sung YE. Electrochromic properties of one-dimensional tungsten oxide nanobundles. Sol Energy Mater Sol Cells 2008;92:179.
[15] Susanti D, Diputra AA Gede Pradnyana, Tananta L, Purwaningsih H, Kusuma GE, Wang C, et al. WO_3 nanomaterials synthesized via a sol-gel method and calcination for use as a CO gas sensor. Chem Sci Eng 2014;8(2):179–87.
[16] Chacón Cecilia, Rodríguez-Pérez Manuel, Oskam Gerko, Rodríguez-Gattorno Geonel. Synthesis and characterization of WO_3 polymorphs: monoclinic, orthorhombic and hexagonal structures. J Mater Sci: Mater Electron 2015;26:5526–31.
[17] Kalhori H, Ranjbar M, Salamati H, Coey JMD. Flower-like nanostructures of WO_3: Fabrication and characterization of their in-liquid gasochromic effect. Sensors Actuat B 2016;225:535–43.
[18] Huang R, Shen Y, Zhao L, Yan M. Effect of hydrothermal temperature on structure and photochromic properties of WO_3 powder. Adv Powder Technol 2012;23:211–4.
[19] Nagy Davidne, Nagy David, Szilagyi Imre Miklos, Fan Xianfeng. Effect of the morphology and phases of WO_3 nanocrystals on their photocatalytic efficiency. RSC Adv 2016;6:33743.
[20] Yoon S, Jo C, Noh SY, Lee CW, Song JH, Lee J. Development of a high performance anode for lithium ion batteries using novel ordered mesoporous tungsten oxide materials with high electrical conductivity. Phys Chem Chem Phys 2011;13:11060–6.
[21] Tian Y, Cong S, Su W, Chen H, Li Q, Geng F, et al. Synergy of $W_{18}O_{49}$ and polyaniline for smart supercapacitor electrode integrated with energy level indicating functionality. Nano Lett 2014;14:2150–6.
[22] Shinde PA, Lokhande AC, Chodankar N, Patil AM, Kim JH, Lokhande CD. Temperature dependent surface morphological modification of hexagonal WO_3 thin films for high performance supercapacitor application. Electrochim Acta 2017;224:397–404.
[23] Shinde PA, Lokhande VC, Chodankar N, Ji TS, Kim JH, Lokhande CD. Enhanced electrochemical performance of monoclinic WO_3 thin film with redox additive aqueous electrolyte. J Colloid Interface Sci 2016;483:261–7.
[24] Shinde NM, Jagadale AD, Kumbhar VS, Rana TR, Kim JH, Lokhande CD. Wet chemical synthesis of WO_3 thin films for supercapacitor application. Korean J Chem Eng 2015;32:974.
[25] Orel B, Opara Krasovec U, Groselj N. Gasochromic behavior of sol-gel derived Pd doped peroxopolytungstic acid (W-PTA) nano-composite films. J Sol-Gel Sci Technol 1999;14:291–308.
[26] GueÂry C, Choquet C, Dujeancourt F, Tarascon JM, LasseÁgues JC. Infrared and X-ray studies of hydrogen intercalation in different tungsten trioxides and tungsten trioxide hydrates. J Solid State Electrochem 1997;1:199–207.
[27] Salje Ekhard. Lattice dynamics of WO_3. Acta Cryst 1975;A31:360.
[28] Wang J, Polleux J, Lim J, Dunn B. Pseudocapacitive contributions to electrochemical energy storage in TiO_2 (anatase) nanoparticles. J Phys Chem C 2007;111:14925.
[29] Huanga Yu, Li Yang, Zhang Guoyang, Liu Wei, Li Dan, Chen Rongsheng, et al. Simple synthesis of 1D, 2D and 3D WO_3 nanostructures on stainlesssteel substrate for high-performance supercapacitors. J Alloys Comp 2019;778:603–11.
[30] Jin Li-Na, Liu Ping, Jin Chun, Zhang Jia-Nan, Bian Shao-Wei. Porous WO_3/graphene/polyester textile electrode materials withenhanced electrochemical performance for flexible solid-statesupercapacitors. J Colloid Interface Sci 2018;510:1–11.
[31] Liu Xudong, Sheng Guangmin, Zhong Minglong, Zhou Xiuwen. Dispersed and size-selected WO3nanoparticles in carbon aerogel for supercapacitor applications. Mater Des 2018;141:220–9.
[32] Wang Haiping, Ma Guofu, Tong Yongchun, Yang Zirong. Biomass carbon/polyaniline composite and WO_3 nanowire-based asymmetric supercapacitor with superior performance. Ionics 2018;24:3123.
[33] Auer Andrea, Portenkirchner Engelbert, Götsch Thomas, Valero-Vidal Carlos, Penner Simon, Kunze-Liebhauser Julia. Preferentially oriented TiO_2 nanotubes as anode material for Li-Ion batteries: insight into Li-Ion storage and Lithiation kinetics. ACS Appl Mater Interfaces 2017;9:36828–36.
[34] Juan Du, Liu Lei, Yifeng Yu, Zepeng Hu, Zhang Yue, Liu Beibei, et al. Tuning confined nanospace for preparation of N-doped hollow carbon spheres for high performance supercapacitors. ChemSusChem 2018;11:1–8.
[35] Du Juan, Liu Lei, Hu Zepeng, Yu Yifeng, Qin Yuming, Chen Aibing. Order mesoporous carbon spheres with precise tunable large pore size by encapsulated self-activation strategy. Adv Funct Mater 2018;28:1802332.